Quantitative imaging of Young's modulus of solids: A contact-mechanics study

H. Ogi,[a] T. Inoue, H. Nagai, and M. Hirao
Graduate School of Engineering Science, Osaka University, Toyonaka, Osaka 560-8531, Japan

(Received 7 March 2007; accepted 24 March 2008; published online 15 May 2008)

We developed equipment and methods for measuring quantitatively the local Young's modulus of solids. It consists of an electrodeless langasite oscillator and line antennas, and oscillator vibrations are generated and detected contactlessly. A constant biasing force results from oscillator mass and is independent of surface roughness. The effect of material anisotropy on the measured stiffness is theoretically discussed for studying the limitation of the quantitative measurement. The microscopy has been applied to polycrystalline copper, and the measured modulus is compared to calculations based on electron-backscatter-diffraction measurements. Also, we applied it to a duplex stainless steel and an embedded silicon-carbide fiber. The results reveal textured regions, defects with high sensitivity, and even stiffness distribution in a single grain. © *2008 American Institute of Physics.*
[DOI: 10.1063/1.2908437]

I. INTRODUCTION

The elastic stiffness of materials reflects interatomic strength for bond stretching and bond bending. Macroscopically, it involves information on inclusions,[1–4] noncohesive grain bonds,[5] oriented heterogeneous phases,[6,7] and so on. In the case of defective inclusions, the stiffness decreases because the stress concentration around the defects causes larger deformation. Thus, macroscopic elastic stiffness can be used for nondestructive evaluation of defects. The elastic stiffness at a local area is expected to be more sensitive to defects because the volume fraction of defects increases.[8] Also, local stiffness provides us with bond strength at interfaces in composite materials. The local stiffness can be a measure for material reliability, especially for composites. Therefore, extensive efforts have been made to develop methodology to measure the local elastic stiffness. Vibrational measurements have been successfully incorporated into atomic-force microscopy by Yamanaka *et al.*,[9,10] and Rabe and co-workers,[11–13] known as ultrasonic atomic-force microscopy (UAFM) and atomic-force acoustic microscopy (AFAM), respectively. They use the resonance-frequency change of an AFM cantilever contacting the material. Their results have contributed to micro- and nanoscience of materials, but a quantitative measurement has been difficult because the cantilever is not isolated, and other components (piezoelectric transducer, materials at the fixed end, and so on) contribute to the resonator system. Furthermore, the apparent stiffness depends on ambiguous parameters such as the inclination angle of the cantilever, elasticity of the gripping wall, and variable biasing force for contact depending on surface roughness. Scratching the specimen by the tip also requires labyrinthine analysis.

Previously, the present authors developed a measurement method using an isolated langasite oscillator[14] and succeeded in measuring resonance frequency of the oscillator in a noncontacting manner using line antennas.[15] We call this method resonance ultrasound microscopy, or RUM. RUM has showed the ability of quantitative determination of materials' local stiffness,[16,17] although its spatial resolution ($\sim 1\ \mu$m) was inferior to UAFM and AFAM.

One of the most important goals of these contact measurements is to visualize the stiffness quantitatively. Namely, we want to know Young's modulus at a measuring point in the imaging area, hopefully without any calibration. This demand poses three challenges. First, the measurement should be independent of surface roughness. Second, it should be independent of temperature. Third, the vibrating probe should be isolated from any other components, except for the examined specimen.

Besides, we have to study the effect of elastic anisotropy of materials on the measured stiffness, because most materials show local elastic anisotropy. The stiffness was evaluated through change in oscillator resonance frequency caused by specimen contact. A Hertzian contact model was then adopted for converting the frequency change to the stiffness of the material.[18] However, it assumes that the material is elastically isotropic and could not be applied to anisotropic materials. Thus, it is important to know the limitation of the Hertzian contact model and the difference between predicted and actual stiffnesses.

There are three purposes in this study. First, we improve the RUM measurement to achieve higher spatial resolution. Second, we study the effect of elastic anisotropy on the measured stiffness based on the analytical calculation proposed by Willis.[19] This result will be widely available for all other contact measurements studying elastic properties in local regions. Third, we discuss capability and limitation of the quantitative measurement with the contacting probe, comparing the measured results with theoretical predictions for various materials.

[a]Electronic mail: ogi@me.es.osaka-u.ac.jp.

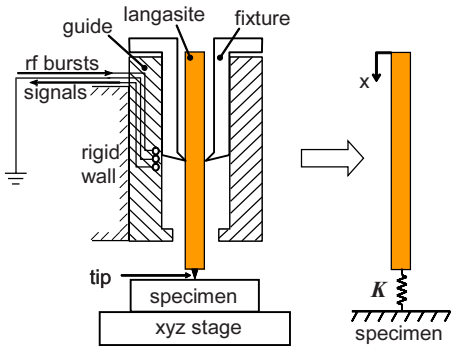

FIG. 1. (Color online) Schematic of the langasite probe with a diamond tip (left), and the vibrational model with the contact spring representing the contact stiffness K between the tip and the specimen (right).

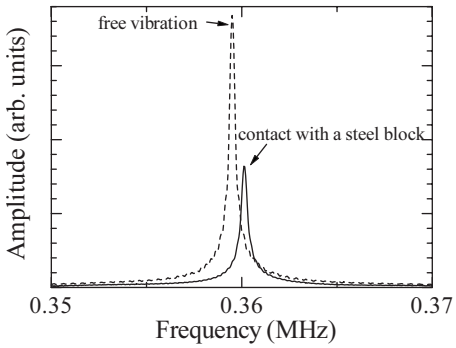

FIG. 2. Resonance spectra measured by the line antenna at a noncontacting state and in contact with a low-carbon steel specimen.

II. MEASUREMENT SETUP

Figure 1 shows the schematic of the langasite oscillator, which is largely the same design in the previous study.[15] However, mass reduction has been made and the whole mass of the probe (including the fixture) is one-tenth that of the pervious one, leading to higher spatial resolution (~200 nm). A monocrystal rectangular parallelepiped langasite ($6.0\times0.68\times0.68$ mm^3) is supported by a nylon fixture at the nodal point, which was identified by the Rayleigh–Ritz method with Lagrangian minimization.[20] The longitudinal direction of the crystal is selected to be along the X direction of the trigonal system for three reasons. First, the X-direction Young's modulus $E_{[100]}$ of langasite takes a minimum value ($E_{[100]}=114$ GPa and $E_{[001]}=198.6$ GPa), providing the highest sensitivity to the contact stiffness as shown below. Second, the temperature derivative of Young's modulus is smaller in the X direction $[(dE_{[100]}/dT)/E_{[100]}=2.8\times10^{-5}$ and $(dE_{[001]}/dT)/E_{[001]}=1.1\times10^{-4}$ (Ref. 21)], yielding stable resonance frequency and resulting in a calibration-free measurement for the temperature change. Third, the longitudinal vibration along the X direction is easily excited by applying the quasistatic electric field in the X direction, owing to the large absolute value of the piezoelectric coefficient, e_{11}.[20] A conical monocrystal diamond tip is attached at the center of the bottom surface of the oscillator to make contact with the specimen, where the vibrational amplitude takes a maximum. Scanning-electron-microscopy observation showed the tip radius to be about 2 μm. A cylindrical guide surrounding the fixture allowed only vertical movement of the probe. Thus, the biasing force for the contact is kept unchanged, being independent of surface roughness; it principally equals the oscillator mass together with the fixture (0.59 mN).

The line antenna consists of generation wire, detection wire, and a grounding wire. It is embedded in the guide. We applied tone-burst voltages to the generation wire to radiate the quasistatic electric field in the X direction at the nodal line of the side face of the crystal, where the maximum stress occurs for an intended resonance. The electric field along the longitudinal direction predominantly causes longitudinal vibrations (A_g vibration groups[22]). After the excitation, the detection wire picks up resonance vibration through the piezoelectric effect.[23,24] A frequency scan yields the resonance spectrum contactlessly, and the Gaussian-function fitting provides the resonance frequency. Figure 2 shows resonance spectra measured before and after contact with a low-carbon steel. Because this frequency scanning requires relatively longer time, we monitored the phase of the received signal at a fixed frequency to determine the resonance-frequency change from the linear relationship between the phase and frequency near the resonance frequency.[24,25]

At each measuring point, resonance frequency at a noncontacting state was first measured; resonance frequency at the contacting condition was measured by lifting the specimen up to make a contact, and the frequency change between them was recorded. Then, the probe was separated from the specimen, and the stage moved the specimen to the next measuring point. The probe does not scratch the specimen surface.

III. CONTACT STIFFNESS FOR ANISOTROPIC SOLIDS

The isolated oscillator in the RUM measurement allows simple and accurate vibrational analysis. The resonator system consists of the oscillator and a spring connecting the oscillator and the specimen (Fig. 1). The spring constant is characterized by the contact stiffness, K, which depends on elastic constants of the tip and specimen, the biasing force, and the tip radius. Assuming a simple-bar resonance, we derived a frequency equation of the oscillator in contact with a specimen[15]

$$\beta L\tan(\beta L)=\frac{K}{K_{\mathrm{osc}}}\equiv p. \tag{1}$$

Here, β is the wavenumber and $K_{\mathrm{osc}}=E_{[100]}A/L$ is the spring constant of the oscillator for a static load. A and L are the cross-section area and the length of the langasite crystal, respectively. p represents the contribution of the contact stiffness to the resonator system; larger p causes larger frequency change. As mentioned, we selected the X axis of the langasite crystal to be vertical because the X-direction Young's modulus $E_{[100]}$ of langasite is the smallest to provide the largest p value. Equation (1) applies when the oscillator is of a long-thin shape. Figure 3 shows the relationship between the frequency change and the contact stiffness for the langasite oscillator used in this study. The broken line is the exact calculation for the A_g-1 mode by the Rayleigh–Ritz method,[26] and the solid line is derived from Eq. (1). Their

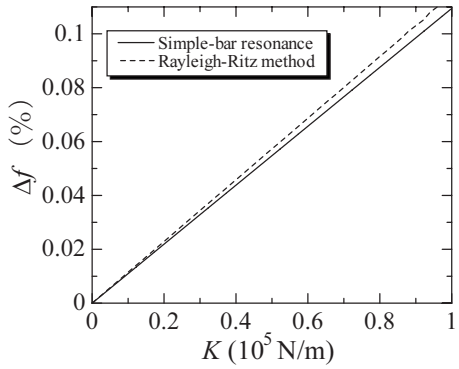

FIG. 3. Relationship between the frequency change and the contact stiffness K for langasite crystal of $0.68\times0.68\times6.0$ mm^3. The broken line is calculated by the Rayleigh–Ritz method with sufficiently larger number of basis functions for the case that the contact spring is exactly placed at the center of the bottom surface of the crystal (Ref. 26). The solid line is calculated by Eq. (1), assuming a simple-bar resonance.

difference is insignificant and we used Eq. (1) for inversely determining the contact stiffness from the measured frequency change. Thus, we can evaluate the local stiffness from only the measured frequency change, when we know the relationship between the contact stiffness (K) and the elastic constants of the specimen.

Willis[19] analyzed the elastic field caused by contact between an indenter and an anisotropic half-space solid using Fourier transformation. Following his analytical method, here, we derive the contact stiffness for anisotropic solids and study the effect of elastic anisotropy on the measured Young's modulus.

We take a Cartesian coordinate system, where the x_3 axis is along the depth direction toward the half space of the contacting specimen. The x_1-x_2 plane defines the specimen surface. The origin is located on the specimen surface and corresponds to the center of the contact area. The contact area is assumed to be an ellipse, whose major and minor axes are denoted by a_1 and a_2, respectively. The pressure distribution at the contact interface is assumed to be expressed by $p_0\sqrt{1-x_1^2/a_1^2-x_2^2/a_2^2}$ with the maximum pressure p_0 at the center.[19] Distributions of displacements $\mathbf{u}(x_1,x_2,x_3)$ are calculated by solving the equilibrium equation with respect to boundary conditions of the free surface and the normal biasing force on the plane of $x_3=0$, performing Fourier transformation for displacements about x_1 and x_2 directions. The resultant expression of the surface displacement of the specimen along the vertical direction, u_3^{spe}, takes the form

$$u_3^{\mathrm{spe}}(x_1,x_2,0)=\frac{3F}{8a_1}\int_0^{2\pi}G_3^{\mathrm{spe}}(\epsilon\cos\theta,\sin\theta)\left\{1-\left(\frac{\cos\theta}{a_1}x_1+\frac{\sin\theta}{a_2}x_2\right)^2\right\}d\theta, \tag{2}$$

where F is the total biasing force at the contact area and $\epsilon=a_1/a_2$ the aspect ratio. G_3^{spe} is the Green function indicating the surface displacement along the x_3 axis caused by the unit point force at the origin. In the case of a contact between transversely isotropic bodies, G_3^{spe} simplifies

$$G_3^{\mathrm{spe}}(\xi_1,\xi_2)=\frac{C^{\mathrm{spe}}}{\sqrt{\xi_1^2+\xi_2^2}}, \tag{3}$$

where C^{spe} denotes a constant determined by the elastic constants of the specimen. The displacement in the tip, u_3^{tip}, is analogously calculated. The relative vertical displacement of the contact interface δ is then determined by $\delta=u_3^{\mathrm{spe}}+u_3^{\mathrm{tip}}-S^{\mathrm{spe}}(x_1,x_2)-S^{\mathrm{tip}}(x_1,x_2)$, where S expresses the surface of contact bodies before deformation. Considering the contact with two spherical bodies (infinite radius for the specimen), we obtain the following relationships:

$$\delta=\left\{\frac{9I_0^3}{128RI_1}F^2\right\}^{1/3}, \tag{4}$$

$$I_0=\sum_{\lambda}^{\mathrm{spe,tip}}\int_0^{2\pi}G_3^{\lambda}(\epsilon\cos\theta,\sin\theta)d\theta, \tag{5}$$

$$I_1=\sum_{\lambda}^{\mathrm{spe,tip}}\int_0^{2\pi}G_3^{\lambda}(\epsilon\cos\theta,\sin\theta)\cos^2\theta d\theta. \tag{6}$$

R is the tip radius. Equation (4) indicates the nonlinear response of the indentation for the applied force F, but in the case of a dynamic measurement with a small amplitude, we can define the contact stiffness K by taking perturbations of δ and F as[27]

$$K=\left(\frac{48RFI_1}{I_0^3}\right)^{1/3}. \tag{7}$$

The aspect ratio ϵ can be determined inversely by an iteration calculation.[28] However, this value differs little from unity for a variety of materials, and we consider that $\epsilon=1$ for our calculation, indicating a circular contact area.

The contact stiffness depends on all components of the elastic constants of the specimen. However, when we evaluate a specimen's stiffness from the resonance frequency, it is important to know which component dominates the contact stiffness K. The difference of the actual and predicted stiffnesses shows the limitation of the quantitative measurement. The effective Young's modulus of the specimen, E_{iso}^*, has been evaluated by the Hertzian contact model, assuming isotropic contacting bodies:

$$E_{\mathrm{iso}}^*=\sqrt{\frac{K^3}{6FR}}=\left(\frac{1-\nu_{\mathrm{spe}}^2}{E_{\mathrm{spe}}}+\frac{1-\nu_{\mathrm{tip}}^2}{E_{\mathrm{tip}}}\right)^{-1}. \tag{8}$$

Here, E and ν are Young's modulus and Poisson's ratio of the isotropic materials. From Eq. (7), we define the effective stiffness, E_{aniso}^*, for anisotropic materials as

$$E_{\mathrm{aniso}}^*=\sqrt{\frac{8I_1}{I_0^3}}. \tag{9}$$

When we make a frequency measurement and obtain the corresponding contact stiffness K, the effective Young's modulus is deduced from Eq. (8). However, the actual modulus is given by Eq. (9).

Figure 4(a) shows comparison of E_{aniso}^* with several moduli of various cubic and hexagonal materials in contact with an isotropic diamond tip as an indenter ($E_{\mathrm{tip}}=1132$ GPa and $\nu_{\mathrm{tip}}=0.067$). In the calculation of E_{iso}^*, we

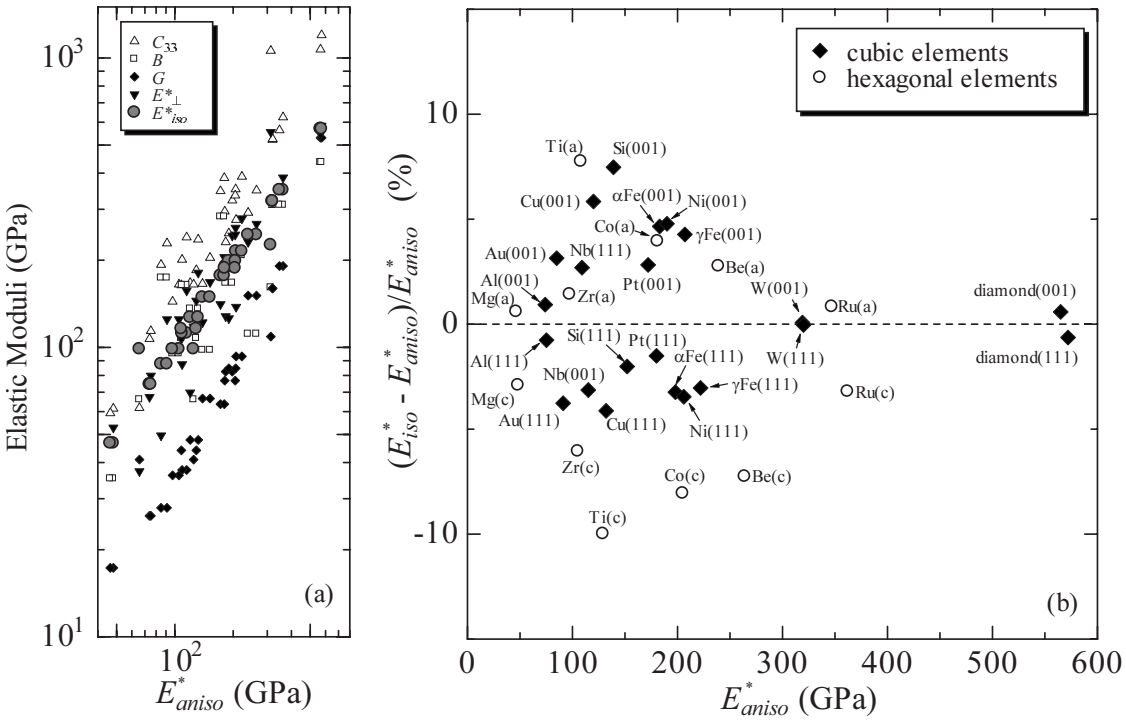

FIG. 4. (a) Correlation of the effective Young's modulus for anisotropic materials (E^*_{aniso}) with elastic moduli for the normal deformation of various cubic and hexagonal elements on their principal planes: C_{33}, B, G, $E^*_\perp$, and E^*_{iso} denote the longitudinal-wave modulus in the x_3 direction, the bulk modulus, the isotropic shear modulus, the effective stiffness derived from the normal Young's modulus, and the effective Young's modulus for isotropic material. (b) The difference between E^*_{aniso} and E^*_{iso} for cubic and hexagonal elements. The notations (a) and (c) for hexagonal elements denote planes perpendicular and parallel to the basal plane, respectively.

calculated E_{spe} and ν_{spe} using the Hill averaging method.[29] Also, we calculated the effective stiffness using the normal Young's modulus instead of E_{spe}, because the principal deformation occurs in the vertical direction and one may consider this modulus to be dominant. (The normal Young's modulus is given from $1/s_{33}$, where s_{33} denotes the component of the compliance matrix of the given crystallographic orientation.) We denote this $E^*_\perp$. Among those various moduli related with the normal deformation, E^*_{iso} shows the best correlation with the actual contact modulus E^*_{aniso}. Thus, the stiffness measured by an indenter nearly provides us with the stiffness of aggregated structure around the contact area. However, there are still discrepancies between E^*_{aniso} and E^*_{iso} as shown in Fig. 4(b): a 10% error could be result from material elastic anisotropy. Figure 5 shows a correlation between their difference and the anisotropy of the longitudinal-wave modulus C_{33}/C^{ave}_{11}, where C^{ave}_{11} denotes the transversely averaged modulus for C_{11} about the x_3 axis, indicating the averaged in-plane modulus.[5] The good correlation in Fig. 5 shows that the longitudinal-modulus anisotropy dominates the error in E^*_{iso}. [This anisotropy shows better correlation than the usual shear-wave anisotropy factor $A=2C_{44}/(C_{11}-C_{12})$.]

IV. QUANTITATIVE YOUNG'S MODULUS MAPPING

Our final goal is to make a calibration-free measurement, that is, measurement of a material's Young's modulus from only the resonance-frequency change without using reference specimens. The measured frequency change can be converted into the contact stiffness K unambiguously by Eq. (1). Then, the effective Young's modulus E^*_{iso} is determined by Eq. (8), which is used to deduce Young's modulus E_{spe} assuming Poisson's ratio [ambiguity of Poisson's ratio is insignificant as seen in Eq. (8)]. However, conversion of K into E^*_{iso} involves one parameter RF, which must be determined by some means. The biasing force F will be measured from masses of the probe and the surrounding fixture, although it

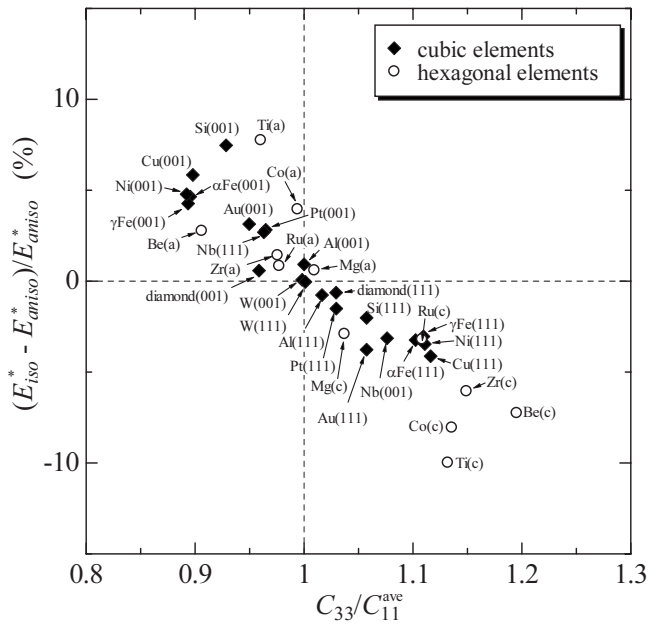

FIG. 5. Correlation between anisotropy of the longitudinal-wave modulus and the error of the evaluated stiffness.

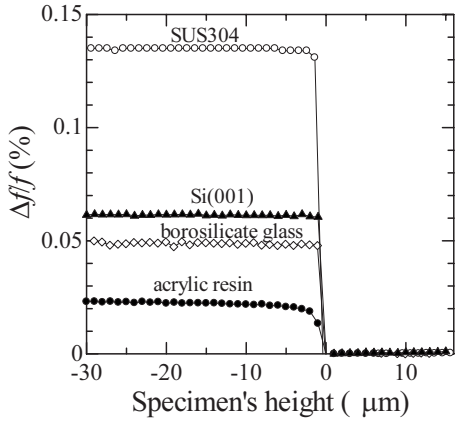

FIG. 6. Changes in resonance frequency caused by contact with various materials. After the contact, the frequency remains nearly constant, being independent of the specimen's height.

may be shifted because of friction between the fixture and the cylindrical guide. We have to pay much more attention to ambiguity of the tip radius because its shape inevitably changes after a large number of indentation measurements, no matter what tip we use, even a diamond tip, the hardest material. Thus, we have to study their effects and propose a way to determine the parameter *RF*.

A. Biasing-force stability

The biasing force F affects the contact stiffness and it must be unchanged over the scanning area for quantitative evaluation of the stiffness. However, UAFM and AFAM methods use AFM cantilevers, and the biasing force varies depending not only on surface roughness but also on the specimen stiffness itself because the deflection angle is changed. Furthermore, their contact-scratch scanning procedure causes additional friction forces at the contact interface, and the evaluation of the total force is never straightforward. Therefore, it has been an important challenge to make the biasing force unchanged. In the RUM setup, the biasing force is applied by gravity, and it will remain unchanged, being independent of the surface roughness. To confirm this, we measured the resonance frequency of the langasite probe, by changing the height of the specimen. The result is shown in Fig. 6. The resonance frequency jumps at the contacting point, but it subsequently levels off while the specimen height changes, demonstrating that the RUM method is insensitive to the specimen height after contact. (Viscoelastic effect occurs with acrylic resin.) Therefore, even if the biasing force changes at each setting because of the friction between the fixture and the guide, it remains unchanged during a single scan.

B. Tip radius

The tip radius can be evaluated from scanning electron microscopy observation, and we measured it to obtain $R=2$ μm. However, this value can vary after many indentations. Now, we propose two methods for determining the parameter *RF*. First, we use a calibration curve for a specimen with no information about its elastic constants. For establishing such a calibration curve, we measured the resonance frequency change for various materials, whose elastic constants are well known. Figure 7 shows the relationship between the effective Young's modulus and the resonance frequency change for them. The error bars represent standard deviations of 100 measurements on different points. The larger error bar for the tungsten-carbide specimen arises from the fact that the examined specimen was a sintered (porous) material and its local stiffness depends highly on the position as will be shown below for a SiC specimen. Dashed and solid lines denote theoretical calculations with Eqs. (1), (7), and (9). We find that $R=2.8$ μm gives a good agreement with measurements. We determined the fitting parameter in this manner before examining the specimen.

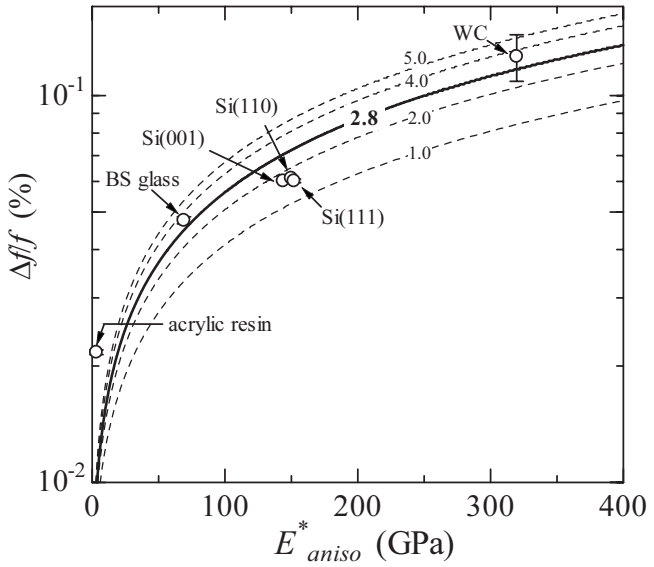

FIG. 7. Relationship between the effective Young's modulus and the resonance-frequency change for contact with various materials. Solid and broken lines are calculations. The numbers are the tip radii in μm used in calculations.

The second possible method is applied for a specimen that includes well-known material in the scanned area. The parameter is fitted so as to provide the known Young's modulus for the known-material region.

V. MAPPING RESULTS AND DISCUSSIONS

A. Polycrystalline copper

First, we show the result for a polycrystalline copper to demonstrate the quantitative measurement of the RUM system, compared to the prediction on the basis of the electron-backscatter-diffraction (EBSD) measurement. The crystallographic orientation was measured every 5 μm and we calculated the effective modulus at each point from Eq. (9). (Details of the EBSD measurements appear elsewhere.[16,17]) Figures 8(a)–8(c) are images obtained by the diffraction quality (DQ), indicating crystallinity of the examined area, the effective stiffness calculated from the EBSD result, and the effective stiffness measured by RUM. The DQ shows low values at grain boundaries because of lattice distortion. The parameter *RF* was determined so that the average of the measured stiffness over 100 grains agrees with the effective stiffness for isotropic copper obtained by the Hill averaging

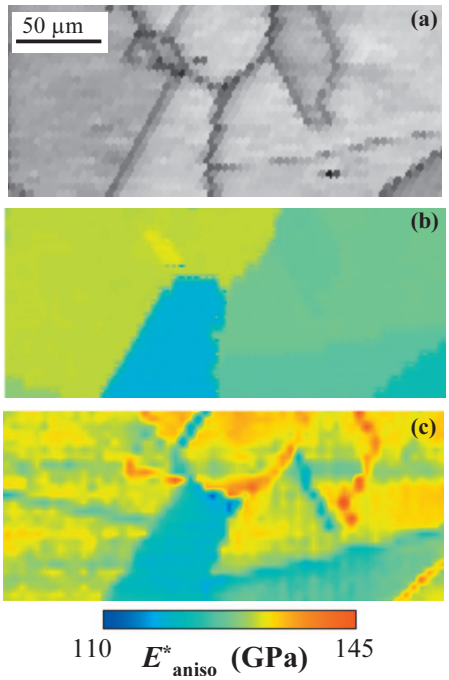

FIG. 8. (Color) (a) Diffraction-quality image obtained by the EBSD method, (b) the stiffness distribution calculated from crystallographic orientations determined using EBSD, and (c) the effective stiffness image obtained by RUM. The color bar is applicable for both (b) and (c).

method for reported monocrystal elastic constants[30] assuming no texture. The measured distribution agrees with that of the calculation. Some grains showed stiffened and softened boundaries as seen in Fig. 8(c). The cause is unknown but highly distorted lattice near the grain boundary could cause unusual elasticity because of anharmonic interatomic potential. Figure 9 compares measured and calculated effective stiffness for many grains. Most grains showed agreement between them within the error limit about 15%. However, some grains showed stiffness much lower than prediction, beyond the possible error caused by elastic anisotropy in Fig. 4(b). Such a softened grain was previously observed for another copper specimen;[16] it might arise from highly distorted grains and dense dislocations; its origin represents an important future research topic. The overall error limit of 15% is reasonable because of the high elastic anisotropy of copper [Fig. 4(b)]. This result is obtained only from the measured

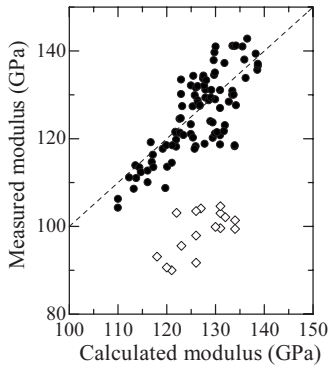

FIG. 9. Comparison between calculated (E^*_{aniso}) and measured (E^*_{iso}) effective stiffnesses for many grains of a polycrystalline copper. Open marks show softened grains.

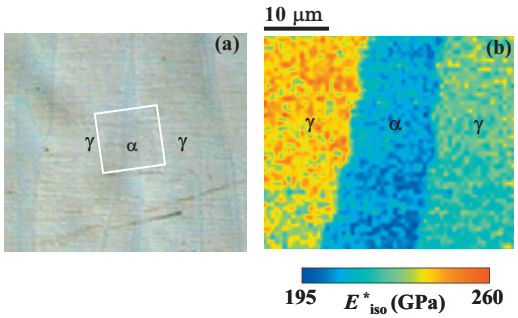

FIG. 10. (Color) (a) Image by optical microscopy and (b) the effective Young's modulus image measured by RUM for a duplex stainless steel. The modulus mapping has been done every 500 nm. The white rectangle in (a) shows the scanned area.

frequency change and one fitted parameter *RF* determined from the reported stiffness of monocrystal copper, showing that the contact-stiffness model presented by Willis applies well, and that the RUM measurement shows quantitative sensitivity to a material's elastic modulus.

B. Duplex stainless steel

Figure 10 shows the optical-microscopy image and Young's modulus image for a duplex stainless steel (JIS-SCS14A). It is a dual-phase material, consisting of ferrite-phase (α) matrix and austenite-phase (γ) island precipitates.[31,32] The frequency change was measured every 500 nm. In this case, we determined the parameter *RF* from the calibration curve in Fig. 7 ($R=2.8$ μm).

Table I shows the elastic constants of pure irons. Young's moduli vary by more than 50%, depending on the crystallographic orientation for both phases. However, the effective Young's modulus of γ-phase precipitate is expected to be larger than that of α-phase matrix, which is demonstrated by the RUM image. Our previous study[17] suggested the stiffness distribution in γ-phase grains. Here, we see more clearly this phenomenon with the higher-resolution RUM: The stiffness distribution in a γ-phase grain is clear, and the effective Young's modulus varies by 5%–10% in a single grain. We attribute this to nonuniformly dissolved chromium atoms. Substitutional impurity atoms decrease the elastic modulus, and this effect depends on the amount of dissolved impurity atoms.[34]

C. Silicon-carbide fiber

Finally, we show the stiffness distribution on a cross section of a silicon-carbide fiber (SCS-6) embedded in Ti-alloy matrix. As shown in Fig. 11, it principally consists of four components:[35] a carbon core, inner carbon coating, chemical vapor deposition (CVD)-deposited β-SiC, and outer carbon coating. The parameter *RF* was determined us-

TABLE I. Young's moduli (GPa) of fcc iron (Ref. 33) and bcc iron (Ref. 33) in the principal directions.

	$E_{[100]}$	$E_{[110]}$	$E_{[111]}$	E_{spe}	E^*_{iso}
bcc Fe	132	220	283	211	192
fcc Fe	142	250	335	242	215

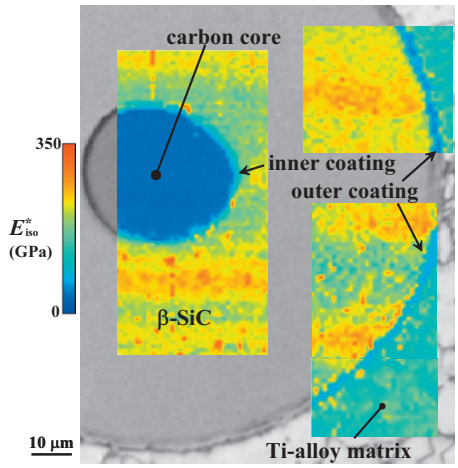

FIG. 11. (Color) Effective Young's modulus mapping images on a single embedded SiC fiber overlapped on the optical-microscopy image.

ing the measurement of the Ti-alloy region (E^*_{iso}=116 GPa) as the reference, which provided R=3.15 μm for the measured biasing force F=0.59 mN. In Fig. 11, we overlap the stiffness images on the optical image of the cross section of the single fiber.

The microstructure of individual components was studied by transmission-electron microscopy in detail by Ning and Pirouz.[35] First, we discuss Young's modulus distribution in carbon regions. The inside region of the core consists of blocks of turbostratic carbon (TC) with 1–50 nm size, whose chemical bonds are similar to those of graphite. The TC blocks are randomly oriented there. However, the inner carbon coating (~1.5 μm thick) consists of TC blocks with 30–50 nm size, and their c axes are predominantly aligned along the radial direction. The basal plane, along which the covalent bonds appear, is in alignment with the longitudinal direction. The microstructure of the outer carbon coating (~3 μm thick) is similar to that of the inner carbon coating, but it consists of finer TC blocks with 1–2 nm size and contains SiC particles. These microstructures suggest higher stiffness in the inner-carbon-coating region because of the texture and in the outer-carbon-coating region because of the texture and SiC particles than that of the carbon core. Figure 12 shows a line trace of the effective Young's modulus in the radial direction, showing larger stiffnesses in inner and outer coating regions. (Because of the limitation of the stroke of the nanostage, three strokes of scanning were made to cover different portions.)

Second, we note a lower Young's modulus in the SiC region than expected. Table II shows monocrystal elastic constants of β-SiC, from which we calculate the averaged-over-direction Young's modulus of 447 GPa and the effective modulus of 327 GPa. However, the RUM result provides the effective Young's modulus smaller than 300 GPa in the SiC region, being around 200 GPa. We attribute this result to the nano- and microdefects, which can be involved during the CVD deposition process. In the RUM measurement, the volume of the probing region is estimated to be smaller than 1 μm^3. The local stress field increases the degree of the stress concentration near defects if any and makes the apparent stiffness decrease more significantly than in the case of the application of a uniform-stress field.

To confirm this effect, we measured the stiffness distribution for a bulk sintered SiC. The SiC particles with submicron diameters were hot pressed and sintered. The sintered material was cut into a 6 mm cube. The porosity was 1.8%, which was determined from the mass density. The overall (macroscopic) elastic constants were measured by resonance ultrasound spectroscopy coupled with laser-Doppler interferometry[37,38] (RUS-LDI) as an isotropic material. This yielded a Young's modulus of 432 GPa and an effective stiffness of 320 GPa, smaller than the (nondefective) monocrystal value by only 2%. Then, we measured the stiffness distribution on this material by the RUM method. The average effective modulus was 180 GPa, much smaller than the macroscopic value. Figure 13 shows the histogram of the measured local stiffness for the bulk sintered SiC by the broken line (the total measurement number was more than 10 000). The stiffness of the bulk sintered material shows a broad

TABLE II. Elastic constants of β-SiC (Ref. 36).

C_{11}	C_{12}	C_{44}	E_{spe}	E^*_{iso}
390	142	256	447	327

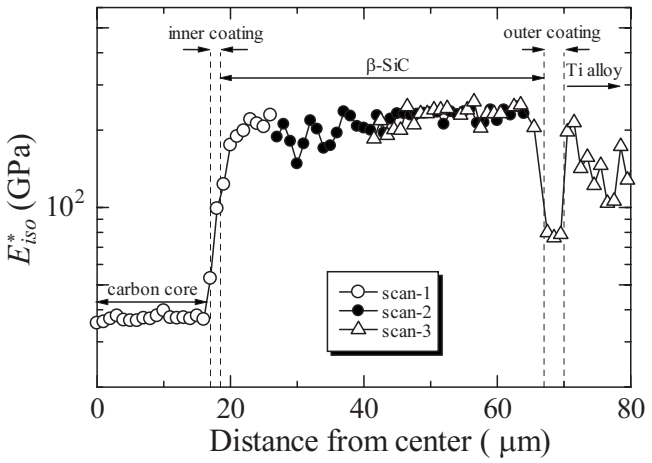

FIG. 12. Variation of the effective stiffness along the radial direction of the fiber. Three independent measurements are shown together.

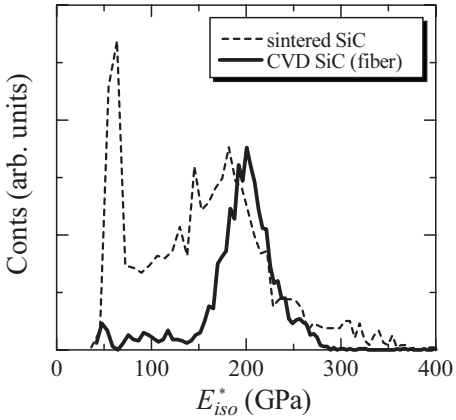

FIG. 13. Histograms of the measured effective stiffness for the sintered SiC material (broken line) and the SiC region of the SCS-6 fiber (solid line).

distribution, involving a high count at very low stiffness (~60 GPa), while it involves high stiffness values (300–330 GPa), corresponding to the effective stiffness of the nondefective bulk material. Therefore, the defects (cavities and incohesive bonds between particles) considerably lower the local stiffness because the local stress field enhances the stress concentration degree around defects more remarkably. However, when the tip touches a single particle, the measurement can provide the inherent stiffness value. The RUS-LDI method uses a wavelength of millimeter scale, giving nearly uniform-stress field for defects, and the stress concentration near defects is less effective.

Such a stiffness decrease at a local region applies for the SiC fiber. In the case of the SiC region of the fiber, we see the narrower distribution as shown in Fig. 13. Thus, we expect much smaller size of defects. Furthermore, the stiffness of the SiC itself can be lowered because the carbon atom content departs from that of the thermodynamically static SiC.[35]

VI. CONCLUSION

RUM has been developed for quantitative measurement of local stiffness of solids. It uses a langasite oscillator and the vibration of the oscillator was excited and detected contactlessly by the line antenna. The oscillator was acoustically isolated, and the surface-roughness effect on the biasing force was minimized by means of a vertically movable probe. Currently, the spatial resolution of RUM is about 200 nm.

The effect of a material's elastic anisotropy on the contact stiffness has been studied, and this reveals that a 10% error could occur in the measured stiffness depending on the anisotropy of the longitudinal-wave modulus rather than the shear modulus anisotropy, or the Zener anisotropy factor.

The correlation of the measurement and the theoretical calculation was confirmed for a polycrystalline copper. The stiffness measured by the RUM method was compared to that calculated from the EBSD result. They agreed within 15% error for most grains, although some grains showed much smaller RUM modulus.

The RUM was also applied to a duplex stainless steel, and it demonstrated the distribution of the stiffness in a single γ-phase grain, suggesting nonuniformly distributed solute Cr atoms.

The stiffness distribution on the cross section of a single SiC fiber was observed in detail. The RUM measurement showed higher stiffness on thin carbon-coating regions. This was explained by the texture and SiC particles involved. The stiffness in the SiC region was significantly smaller than the prediction. This was attributed to small-size defects, which cause stress concentration in the small volume of the RUM measurement, leading to the decrease of the apparent stiffness. Thus, the local stiffness is more sensitive to lattice defects than the macroscopic stiffness.

[1] H. Ledbetter, S. K. Datta, and R. D. Kriz, Acta Metall. **32**, 2225 (1984).
[2] H. Ledbetter and S. K. Datta, J. Acoust. Soc. Am. **79**, 239 (1986).
[3] M. Dunn and H. Ledbetter, J. Acoust. Soc. Am. **99**, 283 (1996).
[4] T. Morishita and M. Hirao, Int. J. Solids Struct. **34**, 1169 (1997).
[5] N. Nakamura, H. Ogi, and M. Hirao, Acta Mater. **52**, 765 (2004).
[6] H. Ogi, N. Nakamura, H. Tanei, R. Ikeda, M. Hirao, and M. Takemoto, Appl. Phys. Lett. **86**, 231904 (2005).
[7] H. Tanei, N. Nakamura, H. Ogi, M. Hirao, and R. Ikeda, Phys. Rev. Lett. **100**, 016804 (2008).
[8] H. Ogi, N. Hayama, H. Niho, M. Hirao, and T. Morishita, IEEE Trans. Ultrason. Ferroelectr. Freq. Control **54**, 1514 (2007).
[9] K. Yamanaka, H. Ogiso, and O. Kolosov, Appl. Phys. Lett. **64**, 178 (1994).
[10] K. Yamanaka, T. Tsuji, A. Noguchi, T. Koike, and T. Mihara, Rev. Sci. Instrum. **71**, 2403 (2000).
[11] U. Rabe and W. Arnold, Appl. Phys. Lett. **64**, 1493 (1994).
[12] U. Rabe, U. K. Janser, and W. Arnold, Rev. Sci. Instrum. **67**, 3281 (1996).
[13] U. Rabe, M. Kopycinska, S. Hirsekorn, J. M. Saldana, G. A. Schneider, J. Phys. D **35**, 2621 (2002).
[14] H. Ogi, J. Tian, T. Tada, and M. Hirao, Appl. Phys. Lett. **83**, 464 (2003).
[15] H. Ogi, H. Niho, and M. Hirao, Appl. Phys. Lett. **88**, 141110 (2006).
[16] H. Ogi, M. Hirao, T. Tada, and J. Tian, Phys. Rev. B **73**, 174107 (2006).
[17] H. Ogi, H. Niho, and M. Hirao, Acta Mater. **54**, 4143 (2006).
[18] J. Tian, H. Ogi, and M. Hirao, J. Appl. Phys. **94**, 6472 (2003).
[19] J. R. Willis, J. Mech. Phys. Solids **14**, 163 (1966).
[20] H. Ogi, N. Nakamura, K. Sato, M. Hirao, and S. Uda, IEEE Trans. Ultrason. Ferroelectr. Freq. Control **50**, 553 (2003).
[21] R. Tarumi, H. Nitta, H. Ogi, and M. Hirao (unpublished).
[22] I. Ohno, Phys. Chem. Miner. **17**, 371 (1990).
[23] H. Ogi, K. Motohisa, T. Matsumoto, K. Hatanaka, and M. Hirao, Anal. Chem. **78**, 6903 (2006).
[24] H. Ogi, K. Motohisa, K. Hatanaka, T. Ohmori, M. Hirao, and M. Nishiyama, Biosens. Bioelectron. **22**, 3238 (2007).
[25] H. Ogi, K. Motohisa, K. Hatanaka, T. Ohmori, M. Hirao, and M. Nishiyama, Jpn. J. Appl. Phys., Part 1 **46**, 4693 (2007).
[26] H. Ogi, T. Tada, J. Tian, and M. Hirao, Jpn. J. Appl. Phys., Part 1 **44**, 4381 (2005).
[27] J. Tian, H. Ogi, and M. Hirao, Appl. Phys. Lett. **87**, 204107 (2005).
[28] S. R. Swanson, Int. J. Solids Struct. **41**, 1945 (2004).
[29] R. Hill, Proc. Phys. Soc., London, Sect. A **A65**, 349 (1952).
[30] H. Ogi, H. Ledbetter, S. Kim, and M. Hirao, J. Acoust. Soc. Am. **106**, 660 (1999).
[31] H. D. Solomon and L. M. Levinson, Acta Metall. **26**, 429 (1978).
[32] S. Tsuchida, Y. Ishikawa, M. Ohtaka, and T. Yoshimura, JSME Int. J., Ser. A **38**, 384 (1995).
[33] H. Ledbetter and S. Kim, *Monocrystal Elastic Constants and Derived Properties of The Cubic and The Hexagonal Elements: in Handbook of Elastic Properties of Solids, Liquids, and Gases* (San Diego, Academic, 2001), Vol. 2.
[34] C. Zener, Acta Crystallogr. **2**, 163 (1949).
[35] X. J. Ning and P. Pirouz, J. Mater. Res. **6**, 2234 (1991).
[36] W. Li and T. Wang, Phys. Rev. B **59**, 3993 (1999).
[37] H. Ogi, K. Sato, T. Asada, and M. Hirao, J. Acoust. Soc. Am. **112**, 2553 (2002).
[38] H. Ogi, T. Ohmori, N. Nakamura, and M. Hirao, J. Appl. Phys. **100**, 053511 (2006).